Title
Three-dimensional myocardial strain correlates with murine left ventricular remodelling severity post-infarction

Journal
Journal of The Royal Society Interface, 16(160)

ISSN
1742-5689

Authors
Soepriatna, Arvin H
Yeh, A Kevin
Clifford, Abigail D
et al.

Publication Date
2019-11-01

DOI
10.1098/rsif.2019.0570

Peer reviewed

JOURNAL OF THE ROYAL SOCIETY INTERFACE

3D Myocardial Strain Correlates with Murine Left Ventricular Remodeling Severity Post-Infarction

Journal:	*Journal of the Royal Society Interface*
Manuscript ID	rsif-2019-0570.R1
Article Type:	Research
Date Submitted by the Author:	30-Sep-2019
Complete List of Authors:	Soepriatna, Arvin; Purdue University, Weldon School of Biomedical Engineering Yeh, Alex; Purdue University, Weldon School of Biomedical Engineering Clifford, Abigail; Purdue University, Department of Animal Sciences Bezci , Semih; University of California Berkeley, Department of Mechanical Engineering O'Connell, Grace ; University of California Berkeley, Department of Mechanical Engineering Goergen, Craig; Purdue University, Weldon School of Biomedical Engineering
Categories:	Life Sciences - Engineering interface
Subject:	Biomedical engineering < CROSS-DISCIPLINARY SCIENCES, Bioengineering < CROSS-DISCIPLINARY SCIENCES, Biomechanics < CROSS-DISCIPLINARY SCIENCES
Keywords:	Infarction, Ischemia-Reperfusion, Left Ventricular Remodeling, Murine, Myocardial Strain, Ultrasound

Author-supplied statements

Relevant information will appear here if provided.

Ethics

Does your article include research that required ethical approval or permits?:
Yes

Statement (if applicable):
The presented study was conducted in accordance with Purdue Universityâ€™s ethical guidelines regarding the use of animals in research. All surgical procedures have been approved by the Purdue Animal Care and Use Committee under protocol number 1505001246.

Data

It is a condition of publication that data, code and materials supporting your paper are made publicly available. Does your paper present new data?:
Yes

Statement (if applicable):
Additional data that support the findings of this study are made available online (doi:10.6084/m9.figshare.9895967).

Conflict of interest

I/We declare we have no competing interests

Statement (if applicable):
CUST_STATE_CONFLICT :No data available.

Authors' contributions

This paper has multiple authors and our individual contributions were as below

Statement (if applicable):
A.H.S. and C.J.G. conceptualized and designed the study. A.H.S. performed all surgical procedures and developed the MATLAB codes for image analysis. A.H.S., A.K.Y., and A.D.C. were responsible for data acquisition, image analysis, and histological analysis. A.H.S., S.E.B., and G.D.O. compared the 3D-DDE strain results with Vic2D. All authors discussed the results and contributed to the writing, editing, and review of the manuscript. All authors gave final approval for publication.

3D Myocardial Strain Correlates with Murine Left Ventricular Remodeling Severity Post-Infarction

Authors:

Arvin H. Soepriatna[1], A. Kevin Yeh[1], Abigail D. Clifford[2], Semih E. Bezci[3], Grace D. O'Connell[3,4], and Craig J. Goergen[1,5]

Affiliations:

[1] Weldon School of Biomedical Engineering, Purdue University, 206 S. Martin Jischke Dr., West Lafayette, IN 47907

[2] Department of Animal Sciences, Purdue University, Creighton Hall, 270 S. Russell Street, West Lafayette, IN 47907

[3] Department of Mechanical Engineering, University of California - Berkeley, 5122 Etcheverry Hall, Berkeley, CA 94720

[4] Department of Orthopaedic Surgery, University of California - San Francisco, 500 Parnassus Avenue, Millberry Union, Suite MU320W, San Francisco, CA 94143

[5] Center for Cancer Research, Purdue University, 201 S. University St., West Lafayette, IN 47907

Corresponding Author:

Craig J. Goergen

cgoergen@purdue.edu

206 S. Martin Jischke Drive, Room 3025

West Lafayette, IN 47907

Phone: (765) 494-1517

Abstract

Heart failure continues to be a common and deadly sequela of myocardial infarction (MI). Despite strong evidence suggesting the importance of myocardial mechanics in cardiac remodeling, many MI studies still rely on 2D analyses to estimate global left ventricular (LV) function. Here, we integrated 4D ultrasound with 3D strain mapping to longitudinally characterize LV mechanics within and around infarcts in order to study the post-MI remodeling process. To induce infarcts with varying severities, we separated fifteen mice into three equal-sized groups: 1) sham, 2) 30-minute ischemia-reperfusion, and 3) permanent ligation of the left coronary artery. 4D ultrasound from a high frequency small animal system was used to monitor changes in LV geometry, function, and strain over 28 days. We reconstructed 3D myocardial strain maps and showed that strain profiles at the infarct border followed a sigmoidal behavior. We also identified that mice with mild remodeling had significantly higher strains in the infarcted myocardium when compared to those with severe injury. Finally, we developed a new approach to noninvasively estimate infarct size from strain maps, which correlated well with histological results. Taken together, the presented work provides a thorough approach to quantify regional strain, an important component when assessing post-MI remodeling.

Keywords: infarction, ischemia-reperfusion, left ventricular remodeling, murine, myocardial strain, ultrasound.

1. Introduction

Coronary artery disease remains the leading cause of death in the United States, with over 1 million acute coronary events predicted to take place in 2019 [1]. Despite recent advances in percutaneous coronary intervention technologies, which have improved patient survival rates, heart failure continues to be a common long-term complication of acute myocardial infarction (MI) with high morbidity and mortality [2]. Cardiac remodeling post-MI encompasses a series of complex molecular, structural, and functional changes in the left ventricle (LV) driven by inflammation, neurohormonal, and mechanical factors [3,4]. Although the short-term effects of remodeling are vital in repairing the damaged myocardium, sustained imbalance between increased hemodynamic load, compromised myocardial mechanics, and impaired cardiac function feeds a pathological response that results in LV dilation and eventual heart failure [3,4]. Specifically, changes in the mechanical microenvironment regulates myofibroblast proliferation and subsequent collagenous scar formation at the infarct border zone, providing the heart with the structural rigidity necessary to minimize infarct expansion and prevent ventricular rupture [4,5]. The developing myocardial scar, although beneficial early in remodeling, reduces LV compliance over time, directly inhibiting LV pumping function [6]. Taken together, the time course, mechanical properties, and size of the myocardial scar tissue are all critical components that determine the fate of the remodeling LV.

Despite strong evidence supporting the importance of myocardial mechanics in remodeling post-MI [5-7], longitudinal assessment of regional LV mechanics proves to be challenging. The majority of *in vivo* infarction studies still rely on 2D image analyses to estimate global metrics of LV function such as ejection fraction and global longitudinal strain [8-10]. These metrics, while valuable in evaluating the overall impact of ischemic injury on cardiac health, do not capture regional differences in myocardial contractility. Furthermore, strain measurements derived from 2D images are sensitive to through-plane motion caused by LV twisting during contraction [11]. Irrespective of these limitations, 2D maps highlighting regional strain differences still provide important spatial and temporal information regarding changes in LV contractility throughout remodeling [12,13].

Recent developments in noninvasive 4D imaging techniques have made it possible for researchers to reconstruct volumetric maps of patient- or mouse-specific LV geometries throughout a cardiac cycle [14-16], opening the possibility for 3D strain mapping of the heart. Indeed, several groups have quantified regional differences in 3D strain in both healthy [17,18] and ischemic LVs [19-21], with results revealing significant strain reductions within infarcted tissue. However, these studies either evaluated strain at only sparse timepoints [19,20] or relied on contrast agents to quantify strain in the remodeling infarct [21]. The reported strain difference between the infarcted and remote myocardium suggests the presence of a strain gradient near infarct border zones that may play an important role in infarct expansion.

A thorough longitudinal study investigating changes in the spatial distribution of 3D myocardial strain in a murine model of acute MI has not yet been conducted. Here, we integrated high resolution 4D ultrasound imaging [14] with 3D strain mapping [19] to monitor cardiac remodeling over 28 days. By employing two surgical mouse models to induce ischemic damage with varying severities, we identified unique remodeling patterns that differed between ischemia-reperfusion and permanent ligation models. By expanding ultrasound strain studies to 3D, we aim to provide further evidence that the mechanical behavior of the LV near infarct border zones contribute to infarct expansion and ventricular remodeling.

2. Materials and Methods

2.1. Coronary Artery Ligation

We randomly assigned fifteen male, wild-type, C57BL/6J mice (age = 14±1 weeks; weight = 27±3 grams; The Jackson Laboratory, Bar Harbor, ME) into three surgical groups: 1) sham (n=5), 2) ischemia-reperfusion (I/R; n=5), and 3) permanent ligation (PL; n=5). For surgery, each mouse was anesthetized with 1-3% isoflurane and endotracheally intubated to a small animal ventilator (SomnoSuite, Kent Scientific, Torrington, CT). Pressure-controlled ventilation supplied air to the lungs with a target inspiratory pressure between 16-18cm H_2O and a peak-end expiratory pressure between 3-5cm H_2O. We secured the mouse to a heated surgical stage and coupled a rectal temperature probe to a homeothermic control module to maintain body temperatures between 36-37°C (RightTemp, Kent Scientific, Torrington, CT). We made a small incision in the 3rd intercostal space of the left thorax and retracted the ribs to expose the LV. The pericardium was dissected to visualize the left coronary artery (LCA). In the sham-operated controls, an 8-0 nylon suture was looped around the LCA without ligating the vessel. In the I/R group, we used a PE-10 tubing in combination with a suture, to temporarily ligate the LCA for 30-minutes before restoring blood flow to the ischemic myocardium (reperfusion) as described previously [22]. In the PL group, the LCA was permanently ligated to induce an infarct [22]. At the end of the procedure, we sutured the incision site and recovered the mouse. All surgical procedures were performed aseptically, and buprenorphine (0.05 mg/kg; ip) was administered as an analgesic. All procedures were approved by the Purdue Animal Care and Use Committee.

2.2. Longitudinal Ultrasound Imaging

All ultrasound images were collected with a Vevo2100 small animal ultrasound system (FUJIFILM VisualSonics Inc., Toronto, Canada) and a 40MHz center frequency linear array transducer (22-55MHz; MS550D). Ultrasound images of the LV were acquired at baseline and on

118 days 1, 2, 3, 5, 7, 14, 21, and 28 post-surgery. **Fig. 1A** summarizes the study design for the presented work. We acquired 4D ultrasound data as described previously [14]. Briefly, successive cardiac and respiratory-gated 2D cine loops were obtained at 1000Hz in short-axis from the apex to the base of the heart by utilizing a linearly translating 3D motor (step size = 0.2mm; **Fig. 1B**). Respiratory waveforms obtained during imaging were used to ensure that ultrasound images were only acquired in between breaths to minimize breathing motion artifacts. Sequential 2D images were then spatially registered, temporally matched based on their relative time in the cardiac cycle, and resampled to isotropic 60μm voxels in MATLAB (MathWorks Inc., Natick, MA). Additionally, we measured mitral valve inflow velocities from the four-chamber view of the heart with pulsed-wave Doppler.

2.3. Ultrasound Image Analysis

2.3.1. Segmentation of Left Ventricular Boundaries

Reconstructed 4D ultrasound data were matched spatially with a custom MATLAB script by utilizing anatomical landmarks such as the sternum, apex, and heart valves. The reoriented 4D data were then loaded into SimVascular for segmentation [23]. First, we created a centerline path from the aortic valve to the apex of the LV and manually segmented the endocardial and epicardial boundaries. 2D segmentations were created at least every 1mm apart, with smaller spacing for regions showing significant changes in geometry. This process was performed at both end-diastole and peak-systole. We also segmented sternal shadowing artifacts to identify regions where strain could not be reliably calculated. Finally, 3D surface models of the endocardial, epicardial, and sternal artifact boundaries at both end-diastole and peak-systole were rendered with uniform meshing (**Fig. 1C**) and exported as STL files for further MATLAB analysis.

2.3.2. Assessment of Global Cardiac Function

The 3D surface models were converted to solid, volumetric meshes and spatially registered to the 4D ultrasound data. We calculated end-diastolic volume (EDV) and peak-systolic volume (PSV) by multiplying the number of voxels in the endocardial solid mesh at the corresponding time point by the isotropic voxel dimensions of the 4D data. These volumes were then used to evaluate global metrics of LV systolic function including stroke volume (SV), ejection fraction (EF), and cardiac output (CO), which were calculated as follows (**Eqs. 2.1-2.3**):

$$SV = EDV - PSV \quad \textbf{(2.1)}$$

$$EF = \frac{SV}{EDV} \text{ x } 100 \quad \textbf{(2.2)}$$

$$CO = SV \text{ x Heart Rate} \quad \textbf{(2.3)}$$

LV diastolic function was also assessed using transmitral flow velocity waveforms obtained from pulsed-wave Doppler. E- and A-wave peak velocities from five different cardiac cycles were measured, and their corresponding averages were used to calculate E/A ratio. We used the E/A ratio to identify whether blood flow into the LV primarily driven by passive filling (pressure gradient caused by LV relaxation; E-wave) or active filling (atrial contraction; A-wave).

2.3.3. Estimation of 3D Maximum Principal Green-Lagrange Strain

We implemented a direct deformation estimation (DDE) algorithm in MATLAB to estimate the 3D deformation gradient tensor as described previously (**Fig. 1D**; [19]). Briefly, we defined a rectangular coordinate grid spaced 5 pixels apart on the 4D ultrasound data. At each grid intersection, an 11x11x11 investigation region was assigned. Using the image at end-diastole as a reference template, we iteratively optimized a warping function that best mapped the affine transformation of this region from the template image to a deformed image at the next timepoint. The warping function was optimized by best matching voxel intensities between the template and deformed image. The warping function was designed to be analogous to the 3D deformation gradient tensor, $\mathbf{F}_{3D}$, such that we could directly estimate $\mathbf{F}_{3D}$ during voxel intensity mapping. This process was repeated until $\mathbf{F}_{3D}$ was determined at each grid intersection *(i,j,k)* across all time points in the cardiac cycle. We then calculated the 3D Green-Lagrange (GL) strain tensor, $\mathbf{E}_{3D}$, as shown in **Eq. 2.4**, where **I** is the second order identity tensor.

$$\mathbf{E}_{3D}^{(i,j,k)} = \frac{1}{2}\left(\mathbf{F}_{3D}^{(i,j,k)^T}\mathbf{F}_{3D}^{(i,j,k)} - \mathbf{I}\right) \qquad \textbf{(2.4)}$$

Finally, the maximum principal component of the 3D GL strain tensor was calculated and superimposed onto the 4D ultrasound data. 3D interpolation was performed to approximate strain values in regions between the coordinate grid points.

2.3.4. *In Vivo* Strain Comparison to Vic2D

In one animal, we compared strain values calculated from the 3D-DDE technique to those measured from Vic2D, a commercially available digital image correlation (DIC) software that has been previously used to quantify tissue strains from clinical images [24,25]. Briefly, representative short-axis slices of the LV were obtained from the isotropic 4D data at baseline and on days 1, 7, and 28 post-permanent ligation of the LCA. Myocardial strains were evaluated with Vic2D by manually selecting a region of interest around the LV wall (ring geometry; 21x21 investigation window, step = 1 pixel). The end-diastolic image was used as the reference configuration. The top 10% of the maximum principal strains in the cardiac cycle were then averaged and compared between the Vic2D and 3D-DDE methods along the anterior and posterior walls of the LV.

2.3.5. Bullseye Mapping of Myocardial Strain

We created volumetric meshes of the myocardial wall by subtracting the rendered endocardial volumes from the epicardial volumes in order to visualize strain within the myocardium (**Fig. 1E**). The mid-surface of the myocardium was obtained by calculating the midpoints between paired endocardial and epicardial boundary points located in a plane normal to the centerline of the LV. We defined paired endocardial and epicardial boundary points as points aligned radially from the centerline of the LV. Myocardial strain values between paired endocardial and epicardial boundary points were averaged together to create a representative mean strain metric. The mid-surface of the myocardium was then unwrapped to polar coordinates, relative to the apex of the LV, to represent the averaged strain values as a bullseye map in accordance with the American Heart Association's 17-segment model (**Fig. 1F**, [26]).

2.3.6. Noninvasive Estimation of Infarct Size

Two approaches to noninvasively estimate infarct size were performed. First, we used myocardial wall thickness at peak-systole as a criterion for determining infarct size. Wall thickness was calculated by measuring the distance between paired endocardial and epicardial boundary points along the LV. Regions with thickness values smaller than 0.5mm were defined to be infarcted as used by others [27]. We then quantified infarct size as the percentage of the myocardium with systolic thickness values below 0.5mm. Infarct size was reported as a percent of LV size to take into account ventricular dilation. This infarct sizing method was only applicable for mice with transmural infarcts (PL) and not for subepicardial infarcts (I/R).

In the second approach, strain profiles were used to estimate infarct size. We first plotted bullseye maps of principal 3D GL strain throughout the cardiac cycle. The maximum strain values at each spatial position were then extracted across all timepoints to construct a representative bullseye map. This step was implemented to account for dyssynchrony in LV contractile patterns in mice with ischemic injury. An initial estimate for infarct center was obtained from the center of the wall-thinned myocardium in the PL group. In the I/R group, which did not exhibit significant wall-thinning, we manually identified the center of low strain regions to identify the infarct center. Strain profiles were then plotted radially from the infarct center, and a sigmoidal fit was implemented across every 30° region (**Fig. 2A-B**). The location of the inflection point was determined to be the boundary of the infarct zone, and spatial strain gradient at the infarct boundary was calculated from the slope of the linear portion of the sigmoidal curve fit. In regions with significant sternal artifacts where the inflection points could not be identified, infarct boundaries were approximated by interpolating adjacent infarct boundaries in polar coordinates. (**Fig. 2C**). Infarct size was then reported as an area percentage in the myocardium that fell within the strain-estimated infarct boundary.

2.4. Histological Analysis

2.4.1. Tissue Preparation for Staining

At the end of the study, we euthanized the mice and perfused 30mM KCl solution to arrest the heart in diastole. Harvested hearts were then sliced to 3-4 uniform segments in short-axis and fixed in 4% paraformaldehyde for 7 days at 4°C before being sent for histology. Briefly, cardiac segments were paraffin-embedded, thin-sectioned (5µm), and stained with hematoxylin-eosin (H&E) and Masson's trichrome (MTC). MTC stain was used to differentiate muscle fibers (red) from collagen-rich scars (blue). We imaged stained tissues in segments at 10x magnification with a LEICA ICC50W stereomicroscope (Leica Microsystems Inc., Buffalo Grove, IL) and quantified collagen content and infarct size using ImageJ [28].

2.4.2. Collagen Quantification and Infarct Sizing

We stitched adjacent cardiac images from a representative slice using MosaicJ [29] and removed image background from the rendered image. MTC images were then separated into their RGB channels to isolate red pixels corresponding to muscle fibers from blue pixels representative of collagen-rich scars. Percent collagen was then calculated as follows (**Eq. 2.5**):

$$\%\ \text{Collagen} = \frac{\#\ \text{blue pixels}}{\text{total}\ \#\ \text{of pixels}}\ \text{x}\ 100 \qquad \textbf{(2.5)}$$

We calculated infarct size from MTC images using a midline length approach [30]. The LV myocardial midline was traced in ImageJ by identifying the midpoints between the endocardial and epicardial boundaries. The midline circumference corresponds to the total midline length. The midline infarct length was measured as the midline arc length in regions where the collagen scar encompassed more than 20% of the myocardial thickness. This 20% threshold was used to represent infarct size in LVs with subepicardial infarcts in the I/R group. Infarct size (IS) was then calculated by dividing the sum of the midline infarct lengths, $l_{infarct}$, by the sum of the total midline length, $l_{total,}$ from all cross-sectional slices of the LV, n (**Eq. 2.6**).

$$\mathrm{IS} = \frac{\sum_{i=1}^{n} l_{infarct}}{\sum_{i=1}^{n} l_{total}} \times 100 \qquad \textbf{(2.6)}$$

2.5. Statistical Analysis

All data were reported as mean ± standard deviation and tested for normality using the Shapiro-Wilk test. We implemented a log transformation on non-normal and heteroscedastic data before running statistical tests. A repeated measures analysis of variance (ANOVA) with post-hoc Tukey's test was performed to study the effects of surgery on cardiac function at the different time points. Similarly, we ran a two-way ANOVA with post-hoc Tukey's test to study the effects of spatial position and surgery on both maximum principal 3D GL strain and collagen content. Lastly, linear regression analyses comparing the different methods of infarct sizing were conducted. All statistical analyses were performed using GraphPad Prism version 8.1.1 (GraphPad Software, San Diego, CA) with $p<0.05$ representing statistical significance.

3. Results

3.1. Longitudinal Assessment of Cardiac Function

254 Long-axis ultrasound images of the LVs from three representative mice are presented at peak-systole in **Fig. 3A**, highlighting geometrical differences between surgical groups. A video of LV motion throughout the cardiac cycle is provided as supplemental material (**Fig. S1**). **Fig. 3A** shows that LV geometry was preserved in the sham group, while myocardial damage was evident in the I/R and PL groups as early as day 1. Akinetic regions, marked in dashed yellow lines, indicated that ischemic injury was primarily localized to the apex of these LVs. A closer inspection revealed that mice in the PL group experienced significant wall thinning and chamber dilation by day 7 post-surgery. We did not observe this trend in mice in the I/R group.

These findings reflected longitudinal changes in global cardiac function (**Fig. 3B-G**). Although all cardiac parameters remained unaffected in the sham group over the course of 28 days, we identified detrimental changes in LV function in the I/R and PL groups. The LVs of mice in the PL group progressively dilated post-surgery until they reached EDVs close to triple that of the sham group at day 28 (EDV_{Sham} = 53±2μL vs. EDV_{PL} = 151±39μL, p<0.01). Interestingly, minimal dilation was observed in the I/R group when compared to the sham group ($EDV_{I/R}$ = 68±8μL, p=0.02). Reductions in LV contractile function due to ischemic injury were detected from day 1 as increases in PSVs that either remained stable in the I/R group or increased proportionally to LV dilation in the PL group (PSV_{Sham} = 18±2μL vs. $PSV_{I/R}$ = 34±9μL, p<0.01; vs. PSV_{PL} = 119±46μL, p<0.01). These resulted in immediate and significant decreases in EFs that remained depressed throughout the study (EF_{Sham} = 66±3% vs. $EF_{I/R}$ = 50±7%, p<0.01; vs. EF_{PL} = 23±12%, p<0.01). Surprisingly, we noticed transient reductions in SV and CO 7 days post-surgery before both returned to baseline values. In addition to compromised systolic function, we also observed significant diastolic dysfunction in the PL group that was not seen in the I/R group (E/A_{Sham} = 1.5±0.3 vs. $E/A_{I/R}$ = 1.3±0.2, p=0.59; vs. E/A_{PL} = 0.5±0.4, p=0.04). Taken together, these results revealed that mice exposed to I/R injuries exhibited smaller degrees of LV remodeling than those subjected to permanent LCA ligation.

3.2. Spatial Distribution of 3D Myocardial Strain

Longitudinal changes in peak-systolic LV geometries and endocardial wall strains from three representative mice are shown in **Fig. 4**. Maximum principal 3D GL strain ($\mathbf{E_I}$) of the endocardial wall was visualized along the anterior and posterior walls of the LV to highlight regional differences in strain, with yellow and blue regions corresponding to areas of high and low strains respectively. Bullseye plots mapping the peak myocardial strain profiles of the unwrapped LV surface are shown in **Fig. 5**, with video representations of day 28 LVs portrayed throughout the cardiac cycle in supplemental material **Fig. S2**. Sternal shadowing artifacts, commonly found near the base of the LV and marked as dashed black lines, artificially lowered strain values in these regions and were excluded from our analysis. Taken together, **Figs. 4-5** illustrate that regions of low strains near the LV apex remained localized in the I/R group but continued to expand proportionally to chamber dilation in the PL group. Furthermore, LV wall thinning was only observed in the PL group, and wall-thinned boundaries continued to expand throughout remodeling, approaching infarct boundaries estimated from the strain profile inflection points.

Representative day 28 long-axis ultrasound images, 3D surface strains, and bullseye strain maps of the remodeled LVs for all mice in the I/R and PL groups are included as supplemental figures (**Figs. S3-S4)**. Day 28 strains along the entire thickness of the LV wall are also provided for one representative mouse in each surgical group in supplemental **Fig. S5**. These supplemental figures highlight substantial heterogeneity in LV remodeling across mice both within and between groups. However, clear patterns are present, and we noticed that most mice exhibited asymmetrical infarcts skewed towards the anterior wall. Lastly, a comparison of maximum principal strain values

300 between the 3D-DDE and Vic2D methods is summarized in supplemental **Fig. S6** for a representative LV with an asymmetrical anterior infarct. Although both techniques successfully captured strain reductions along the infarcted anterior wall when compared to the contractile posterior wall, the 3D-DDE algorithm more appropriately tracked changes in LV boundaries throughout a representative heartbeat, as strain values returned to 0 at end of the cardiac cycle.

305 Interestingly, we identified significant differences in maximum principal 3D GL strain values within the infarcted myocardium between mice in the I/R and PL groups. Strain profiles averaged across all five mice in each surgical group are shown in **Fig. 6A-E**. Throughout the 28 days following surgery, we consistently observed a sigmoidal strain profile at the interface between infarcted and remote myocardium. We also detected significantly higher strain values within the infarcted myocardium of mice in the I/R group when compared to those in the PL group (Day 28: $E_{Infarct,I/R} = 0.22 \pm 0.10$ vs. $E_{Infarct,PL} = 0.09 \pm 0.03$, p=0.01), while sham-operated mice maintained healthy strain values in the LV apex ($E_{Apex,Sham} = 0.40 \pm 0.03$). Conversely, no differences in strain were seen in the remote myocardium between the three groups ($E_{Base,Sham} = 0.41 \pm 0.03$ vs. $E_{Remote,I/R} = 0.42 \pm 0.02$, p=0.97; vs. $E_{Remote,PL} = 0.40 \pm 0.02$, p=0.95). We observed no differences in the spatial strain gradient at the infarct boundary between the I/R and PL groups across all time points (**Fig. 6F**).

3.3. Histological Analysis of Collagen Content and Infarct Size

Representative histology images of mouse LVs stained with MTC revealed varying distributions of collagen-rich, fibrotic (blue) tissues between surgical groups (**Fig. 7A-B**). The 320 absence of fibrosis within the myocardium of sham-operated mice demonstrated that sham surgeries contributed little to no myocardial damage. Significant scarring, however, was observed in both the I/R and PL groups (percent collagen: $Sham_{Apex} = 3 \pm 2\%$ vs. $I/R_{Apex} = 15 \pm 8\%$, p<0.01;

vs. PL_{Apex} = 38±17%, p<0.01). While mice in the PL group developed transmural infarcts, as shown by the presence of collagen spanning the entire thickness of the myocardium, mice in the I/R group interestingly only developed subepicardial scarring. We also noticed an increase in interstitial collagen percentage towards the infarcted apex (percent collagen: $base_{PL}$ = 7±3% vs. mid-$papillary_{PL}$ = 23±6%, p<0.01; vs. $apex_{PL}$ = 38±17%, p<0.01). Finally, we compared infarct sizes estimated from 3D strain maps with those calculated from histology and discovered a strong correlation between the two approaches (**Fig. 7C**; R^2 = 0.93, p<0.01).

3.4. Correlation of Infarct Size

Correlation plots comparing infarct sizes (IS) estimated from three different approaches are summarized in **Fig. 8A-C**. Although we found a strong positive correlation between all methods (R^2 > 0.80, p<0.05), infarct sizes evaluated from histological staining at day 28 were better correlated with strain-estimated infarct sizes (R^2 = 0.95) than those measured from wall-thinning (R^2 = 0.83). Similarly, a stronger negative correlation between strain-estimated infarct size and ejection fraction (R^2 = 0.69; **Fig. 8D**) was observed, while infarct size approximated from wall-thinned regions exhibited only moderate correlation with ejection fraction (R^2 = 0.41; **Fig. 8E**). Interestingly, we identified significant differences in measured infarct size between the strain-estimated and wall-thinned approaches between days 1-3 post-surgery (p<0.05) which appeared to converge throughout cardiac remodeling (**Fig. 8F**).

4. Discussion

We have demonstrated in two mouse models of myocardial infarction that DDE, in conjunction with 4D ultrasound, provides regional *in vivo* estimates of 3D myocardial strain. Unlike 2D techniques, regional strain mapping not only helps explain the observed decrease in global LV function post-injury, but also reveals the importance of strain profiles in driving infarct expansion. Specifically, mice exhibiting higher strain values within infarcted tissue experienced smaller degrees of LV remodeling. Furthermore, our initial myocardial 3D maximum principal strain maps predicted final infarct size four weeks after ischemic injury. Taken together, these strain data help characterize the role that mechanical strain plays in LV remodeling post-infarction.

4.1. Advantages of Direct 3D Strain Estimation

A significant advantage of the 3D-DDE technique is its ability to capture regional strain differences along the entire thickness of the myocardium (**Fig. S5**). Most preclinical [8,10,13] and clinical [11,17] ultrasound studies to date rely on commercially available ultrasound software packages to estimate 2D myocardial strain (ε) as the change in length of a segment, ΔL, divided by its original length, L_0 (**Eq. 4.1**):

$$\varepsilon = \frac{L - L_0}{L_0} = \frac{\Delta L}{L_0} \qquad \textbf{(4.1)}$$

The observed change in length, either in the circumferential, longitudinal, or radial direction, is measured by tracking the endocardial and epicardial LV boundaries throughout the entire cardiac cycle using speckle-tracking algorithms. Since a simple change in length is used to approximate strain within large subregions, this approach cannot resolve regional strain differences within the myocardium. This linear approximation also does not consider the nonlinear components of strain and is only appropriate when estimating small deformations less than 5% [31]. This is not the case in many soft tissues, such as the heart, where large deformations are observed *in vivo*. Finally, as the heart undergoes twisting during systolic contraction, 2D techniques are negatively impacted by through-plane motion [11]. By directly estimating 3D deformation gradient tensor from small image subregions within 4D ultrasound data, these issues can be mitigated.

Another advantage of the presented technique lies in its ability to yield reproducible measures of 3D strain. Unlike existing techniques, which often rely on displacement regularization prior to strain estimation, the DDE method estimates 3D deformation gradient tensor directly during voxel intensity mapping as reported previously [19]. This results in a noise-insensitive algorithm that provides a more accurate and precise strain field estimation when compared to displacement-based methods, as supported by *in silico* validation [19]. We demonstrate the reproducibility of our 3D strain measurements in supplemental **Fig. S7**, which highlights similarities in the bullseye strain maps of all 15 healthy mice imaged at baseline. In all cases, we found high strain values ranging between 0.40-0.45 throughout the LV myocardium, except in regions with prominent sternal artifacts. This suggest that across animals, we are consistently obtaining reproducible values of strain. Additionally, the fact that we observed 1) a consistent sigmoidal behavior between the infarct and remote regions with similar strain values in these regions (**Fig. 6**) and 2) reported a consistent strain-estimated infarct size for each animal at the same location (**Figs. 5&8F**) throughout disease progression further demonstrate the reproducibility of the technique. Taken together, these data suggest that if sternal artifacts are minimized or avoided during image acquisition, 3D myocardial strain in remodeling LV can be reliably quantified.

4.2. 3D Strain Map Reveals Myocardial Tissue Heterogeneity

Through our 3D approach, we can identify regional variations in strain values and profiles that compare well to previously published results. Many 2D ultrasound studies have reported significant decreases in global myocardial strains in mice subjected to infarction, with the remote myocardium exhibiting significantly higher strains than the infarcted tissue [8,10,12]. In the radial direction, where the largest deformation is observed [32], strain values range between 25-40% in the healthy myocardium but drop to less than 15% within the infarct [8,10]. Our 3D strain results are consistent with these findings (**Figs. 6A-E**). Furthermore, a short-axis comparison of maximum

392 principal strains between the presented 3D-DDE technique and Vic2D yielded similar ranges of
393 strain values (**Fig. S6**).

394 Although LV kinematics in the remote and infarct zones have been widely studied, the
395 interface between these regions remains to be fully characterized as previous work has only
396 described intermediate strain values in this vulnerable border zone [12,13]. Unsurprisingly, given
397 the original ultrasound data, heterogeneity in border zone strain patterns can be identified in the
398 reconstructed 3D strain maps (**Figs. 4-5, S2-S5**). These strain patterns are correlated with complex,
399 nonuniform deposition of collagen along LV wall, clearly visualized from histological staining of
400 the midpapillary level of the LV in the PL group (**Fig. 7A**). Indeed, collagen fiber orientations are
401 remarkably heterogeneous in the healing myocardial scar and likely influence the mechanical
402 properties of the infarct border zone [33,34]. Taken together, capturing strain heterogeneity within
403 the infarct border zone early in remodeling may provide important insights into the role of strain
404 in infarct expansion and LV remodeling.

405 **4.3. Correlation Between Strain Profiles and LV Remodeling Severity**

406 Strain profiles near infarct border zones exhibit a unique sigmoidal behavior (**Fig. 6A-E**),
407 likely caused by a spatial decrease in collagen content away from the infarct (**Fig. 7A-B**).
408 Interestingly, throughout the 28 days post-infarction, we found significantly higher strain values
409 within the infarcted myocardium of mice in the I/R group when compared to those in the PL group
410 (**Fig. 6B-E**). A sustained increase in strain within the infarct zone may suggest either a higher
411 percentage of viable cardiomyocytes or an improved scar contractile function attributed to the
412 mechanoregulation of myofibroblast activity [5,35]. Within the damaged myocardium, these
413 elevated strains may be a unique characteristic of small infarcts, but further investigation is
414 necessary to determine its role on infarct expansion during early remodeling.~~play a critical role in~~

~~minimizing infarct expansion during early remodeling, a response that may positively impact patient outcomes.~~ Indeed, we measured significant improvements in both systolic and diastolic LV functions (**Fig. 3B-G**), as well as significantly smaller final infarct sizes (**Fig. 7C**), in the I/R group compared to the PL group. Although direct regional strain comparisons between mice subjected to I/R and PL surgeries have yet to be conducted within a single study, our results closely match findings from existing ultrasound studies, which report a significant increase in infarct size and worse remodeling outcomes with prolonged ischemic durations [36,37].

4.4. Strain Profiles Provide Early Estimates of Infarct Size

A key ~~finding~~ discovery from this study is the propensity for wall-thinned myocardial regions at early stages to expand towards the strain-estimated infarct boundaries (**Fig. 5&8F**). Wall thinning is generally accepted to be the final product of infarct healing, and although the majority of wall thinning in murine models occurs within the first week, this gradual process may continue to take place up to a month post-infarction [6,38]. Additionally, wall thinning is often used to monitor infarct expansion *in vivo* [6], is primarily responsible for LV rupture [38], and directly impacts both systolic and diastolic function [5]. Thus, the ability to early predict the extent of wall thinning noninvasively may provide critical insights into LV remodeling and progression to heart failure.

Our data suggest that~~, as early as day 1,~~ the damaged area with compromised 3D maximum principal strain values is predictive of final infarct size as early as day one. As the strain-estimated infarct size in the PL group remained unchanged throughout ventricular remodeling, rapid expansion of wall-thinned regions was prevalent within the first week before converging with the strain-estimated infarct border (**Fig. 8F**). Other previous work ~~has~~ similarly reported that changes in 2D myocardial principal strain also precede LV wall thinning in a genetic mouse model of dilated cardiomyopathy [39]. A potential explanation for this observation may be related to the creation of a stiff provisional matrix in the ischemic region early in remodeling which facilitates the gradual formation of collagen-rich scars. As nonviable cardiomyocytes are resorbed, a provisional granulation tissue rich in fibrin, laminin, and glycosaminoglycans are quickly formed to provide the LV with temporary structural support [6]. In the presence of a stiff extracellular matrix (ECM), transforming growth factor beta (TGF-β) is released from the latent-associated peptide complex due to increased mechanical resistance to cell tension [40]. TGF-β then promotes the differentiation of cardiac fibroblasts to myofibroblasts, which gradually replace the provisional structure with collagen-rich infarct tissue [6,40]. Thus, the presence of necrotic cardiomyocytes and a stiff provisional structure are likely detected as an immediate decrease in strain values one day after infarction (**Figs. 4-5**). As these regions eventually become collagen-rich scars, a process that take several days or weeks to fully develop, the initial changes in myocardial ECM may explain why early strain-estimated infarct size remains unchanged throughout disease progression and is predictive of final infarct size (**Fig. 8F**).

Our comparison of day 28 infarct sizes calculated from three different approaches revealed that gold-standard histology infarct size is best correlated to strain-estimated infarct size (**Fig 8A-C**). Furthermore, we observed a better correlation with ejection fraction for the strain-estimated infarct size when compared to the wall-thinned approach ($R^2 = 0.69$ vs. $R^2 = 0.41$). These findings indicate that 3D principal strain profiles can be used to accurately predict final infarct size in rodents and may have similar utility in humans. This discovery is impactful because it presents a novel noninvasive method of estimating infarct size without the use of contrast agents or tissue collection. Previously, infarct size can only be reliably estimated using late-gadolinium enhanced MRI [21] or *ex vivo* histological staining [30].

4.5. Limitations

One major limitation of this study is the impact of image quality on strain estimation. Since the 3D-DDE algorithm is a direct image-based approach, shadowing artifacts can affect the measured strain values. As mentioned previously, sternal shadowing artifacts commonly found near the base of the LV resulted in underestimation of strains. Although we addressed this problem by removing these regions from our final strain analysis, care during data acquisition to minimize shadowing artifacts is needed. Another limitation is the computational time needed for the strain analysis. Due to the large number of investigation regions and need to spatially resolve small differences between timepoints, the strain analysis requires 2-3 hours to complete per dataset. It is important, however, to note that a tradeoff exists between processing times and the desired spatial resolution of the analyzed strain. In other words, if less refined strain maps are needed, the computational costs would be reduced dramatically. Lastly, surgical inductions of myocardial ischemia in mice are not true reflections of the gradual series of events leading up to a heart attack in humans. Mice experience smaller increases in collagen content post-MI [38] and undergo substantially faster infarct healing than typically observed in patients [6], which may lead to species-differences in the LV remodeling process. Beyond mice, however, similar strain mapping and profiling techniques could be applied to 4D ultrasound data acquired from other rodents, large animals, and humans.

Although the presented study focused on characterizing changes in 3D maximum principal strain, it is important to note that other metrics including the 2nd and 3rd principal strains, as well as principal strain direction, may provide additional insights into the remodeling process. A previous study using tagged MR imaging of the porcine LV showed significant reductions in all three components of principal strains post-infarction [41]. Regional differences in principal strain directions were also detected; notably, maximum principal strain angles rotated away from the radial direction within the infarcted myocardium and its surrounding region. Future work will be needed to fully characterize the relationship between infarct expansion, principal strain directionality, and other components of the 3D strain tensor.

5. Conclusion

In summary, we have demonstrated a novel and robust approach to noninvasively quantify 3D myocardial strain. By integrating 4D ultrasound with a 3D-DDE technique, we expanded existing 2D ultrasound strain studies to 3D to better characterize the role of myocardial mechanics in disease progression. To the best of our knowledge, this study is the first demonstration of the use of 4D ultrasound to quantify 3D strain in order to characterize regional differences, instead of global changes, between two murine models with different infarct severities. By reconstructing 3D strain maps of the LVs, we were able to capture strain heterogeneity and characterize the sigmoidal strain profile at infarct border zones. We discovered that mice undergoing mild LV remodeling had significantly higher strain values within the infarcted tissue when compared to those with severe remodeling, suggesting that a more contractile infarct scar may be a unique characteristic of small infarcts ~~minimize early infarct expansion~~. Finally, we described a new method to noninvasively estimate and predict final infarct size, without the use of contrast agents, at an acute phase based on 3D strain maps. Taken together, the findings presented in this study highlight the importance of 3D strain when studying how the mechanical behavior of the LV near infarct border zones contributes to post-infarction remodeling. Future work will be needed to investigate if the presented technique can be used to better characterize the role of 3D strains in infarct expansion, infarct extension, and in cases of multiple infarcts.

Ethics. The presented study was conducted in accordance with Purdue University's ethical guidelines regarding the use of animals in research. All surgical procedures have been approved by the Purdue Animal Care and Use Committee under protocol number 1505001246.

Data Accessibility. Additional data that support the findings of this study are made available online (doi:10.6084/m9.figshare.9895967).

Authors' Contributions. A.H.S. and C.J.G. conceptualized and designed the study. A.H.S. performed all surgical procedures and developed the MATLAB codes for image analysis. A.H.S., A.K.Y., and A.D.C. were responsible for data acquisition, image analysis, and histological analysis. A.H.S., S.E.B., and G.D.O. compared the 3D-DDE strain results with Vic2D. All authors discussed the results and contributed to the writing, editing, and review of the manuscript. All authors gave final approval for publication.

Competing Interests. The authors have no conflict of interest to report.

Funding. This work was funded by the Hugh W. and Edna M. Donnan Fellowship (A.H.S.), the American Heart Association through grant 14SDG18220010 (C.J.G.), and the Indiana Clinical and Translational Sciences Institute, funded in part by Grant Number UL1TR001108 from the National Institutes of Health, National Center for Advancing Translational Sciences, Clinical and Translational Sciences Award (C.J.G).

Acknowledgements. The authors would like to thank Drs. John Boyle, Guy Genin, and Stavros Thomopoulos for their feedback on the strain code development. We would also like to thank Kristiina Aasa, Stephen Buttars, and Andrew Needles at FUJIFILM VisualSonics Inc. for their technical assistance with the Vevo2100 ultrasound system.

Figure Captions

Fig. 1: Study design. **(A)** Fifteen adult, male mice were randomly assigned into 3 surgical groups: 1) sham-operated controls, 2) 30-min ischemia-reperfusion (I/R), and 3) permanent ligation (PL) of the left coronary artery (yellow arrow). A Vevo2100 ultrasound system was used to acquire 4D ultrasound data and flow information of the LV at baseline and on days 1, 2, 3, 5, 7, 14, 21, and 28 post-surgery. At the end of the study, the heart was stained with hematoxylin-eosin (H&E) and Masson's trichrome (MTC). Yellow dashed outlines highlight the infarcted myocardium. **(B)** We reconstructed 4D ultrasound data from ECG and respiratory-gated 2D short-axis ultrasound images of the LV. **(C)** 3D endocardial (red), epicardial (blue), and sternal artifact (white) boundaries were segmented at end-diastole and peak-systole. **(D)** Maximum principal 3D Green-Lagrange strain **(E_I)** was calculated using a direct deformation estimation technique. **(E)** Strain was then localized within the myocardium using segmented boundaries and presented as bullseye maps **(F)**. A: anterior, S: septal, L: lateral; B: base. Scalebar: 1mm.

Fig. 2: Strain estimation of infarct size. **(A)** We extracted myocardial strain profiles radially from the infarct center (black crosshair) and performed sigmoidal fitting on strain profiles averaged across every 30° region. **(B)** The spatial positions of the inflection points (square box and black dots) are defined as the infarct border and unwrapped from the infarct center to estimate infarct boundaries in regions with sternal artifacts **(C)**. Infarct size is defined as the percentage of the myocardium that lies within the strain-estimated infarct boundary.

Fig. 3: LV remodeling post-infarction. **(A)** Representative long-axis ultrasound images of mouse LVs taken at peak-systole. ~~The a~~Akinetic myocardial walls, indicative of ischemic damage, are

outlined in dashed yellow lines. Global metrics of LV function **(B-G)** showed that mice in both I/R and PL groups exhibited significant reductions in LV contractile function post-surgery, but significant dilation and diastolic dysfunction were only consistently measured in the PL group. Taken together, mice in the PL group experienced greater degrees of cardiac remodeling when compared to those in the I/R group. Data are shown as mean ± standard deviations (**p*<0.05). I/R: ischemia-reperfusion, PL: permanent ligation. Blue asterisks: PL vs. Sham; Red asterisks: I/R vs. Sham; Purple asterisks: PL vs. I/R. Scalebar: 1mm.

Fig. 4: Longitudinal 3D representations of peak-systolic LV boundaries with maximum principal 3D Green-Lagrange myocardial strains ($\mathbf{E_I}$) overlaid onto the endocardial wall. Epicardial boundaries are shown in gray. Dark blue areas highlight akinetic regions of the myocardium. Scalebar: 1mm.

Fig. 5: Longitudinal bullseye maps of the maximum principal 3D Green-Lagrange strain ($\mathbf{E_I}$) within the myocardium. Strain-estimated infarct boundaries are outlined in solid black lines with infarct centers marked as black crosshairs. Wall-thinned infarct boundaries measured from segmentation are outlined as white dotted lines, while sternal artifacts are outlined as black dashed lines.

Fig. 6: Myocardial strain profiles of the remodeling LVs averaged across mice in each group and plotted at **(A)** baseline and **(B-E)** on days 1, 3, 7, and 28 post-surgery. Strain profiles in nonischemic mice (baseline and sham) are plotted radially away from the LV apex (black x-axis). In ischemic mice, strain profiles are plotted only in regions near infarct boundaries (r = 0; purple

x-axis). Strain values averaged within the infarcted and remote myocardium are shown as the left and right inset bar graphs respectively. **(F)** Strain gradients, calculated within the linear component of the sigmoidal fit from the strain profiles, did not show significant changes between surgical groups over the 28-day period. Data are shown as mean ± standard deviations (*p<0.05).

Fig. 7: Histological analysis of collagen content and infarct size. **(A)** Histology images of mouse LVs, obtained 28 days post-surgery and stained with Masson's Trichrome, revealed subepicardial scarring in the I/R group and transmural infarcts in the PL group. Muscle fibers are stained red while collagen-rich scars are stained blue. **(B)** Bar graphs showing percent collagen highlighted spatial variations in collagen content relative to infarct location. **(C)** Strain-estimated infarct size strongly correlated to infarct size measured from the histological midline length approach. Data are shown as mean ± standard deviations (*p<0.05). Scalebar: 1mm.

Fig. 8: Correlation of varying infarct sizing techniques with cardiac function. **(A-C)** Correlation plots comparing three different infarct sizing methodologies showed that the proposed strain-estimation technique best correlated with gold-standard histological estimation of infarct size. Correlation of **(D)** strain-estimated and **(E)** wall-thinned infarct size with ejection fraction. Linear regression lines are shown as solid black lines with 95% confidence intervals shaded in gray. **(F)** Line graphs summarizing infarct size growth throughout cardiac remodeling. Data are shown as mean ± standard deviations (*p<0.05). Light blue asterisks: wall-thinned PL vs. strain-estimated I/R; Dark blue asterisks: strain-estimated PL vs. strain-estimated I/R; Black asterisks: wall-thinned PL vs. strain-estimated PL.

6. References

[1] Benjamin, E.J., Muntner, P., Alonso, A., Bittencourt, M.S., Callaway, C.W., Carson, A.P., Chamberlain, A.M., Chang, A.R., Cheng, S., Das, S.R., et al. 2019 Heart Disease and Stroke Statistics-2019 Update: A Report From the American Heart Association. *Circulation* **139**, e56-e528. (doi:10.1161/CIR.0000000000000659).

[2] Cahill, T.J. & Kharbanda, R.K. 2017 Heart failure after myocardial infarction in the era of primary percutaneous coronary intervention: Mechanisms, incidence and identification of patients at risk. *World J Cardiol* **9**, 407-415. (doi:10.4330/wjc.v9.i5.407).

[3] Sutton, M.G. & Sharpe, N. 2000 Left ventricular remodeling after myocardial infarction: pathophysiology and therapy. *Circulation* **101**, 2981-2988. (doi:10.1161/01.CIR.101.25.2981).

[4] Cohn, J.N., Ferrari, R. & Sharpe, N. 2000 Cardiac remodeling--concepts and clinical implications: a consensus paper from an international forum on cardiac remodeling. Behalf of an International Forum on Cardiac Remodeling. *J Am Coll Cardiol* **35**, 569-582. (doi:10.1016/s0735-1097(99)00630-0).

[5] van den Borne, S.W., Diez, J., Blankesteijn, W.M., Verjans, J., Hofstra, L. & Narula, J. 2010 Myocardial remodeling after infarction: the role of myofibroblasts. *Nat Rev Cardiol* **7**, 30-37. (doi:10.1038/nrcardio.2009.199).

[6] Richardson, W.J., Clarke, S.A., Quinn, T.A. & Holmes, J.W. 2015 Physiological Implications of Myocardial Scar Structure. *Compr Physiol* **5**, 1877-1909. (doi:10.1002/cphy.c140067).

[7] D'Elia, N., D'Hooge, J. & Marwick, T.H. 2015 Association Between Myocardial Mechanics and Ischemic LV Remodeling. *JACC Cardiovasc Imaging* **8**, 1430-1443. (doi:10.1016/j.jcmg.2015.10.005).

[8] Bhan, A., Sirker, A., Zhang, J., Protti, A., Catibog, N., Driver, W., Botnar, R., Monaghan, M.J. & Shah, A.M. 2014 High-frequency speckle tracking echocardiography in the assessment of left ventricular function and remodeling after murine myocardial infarction. *Am J Physiol Heart Circ Physiol* **306**, H1371-1383. (doi:10.1152/ajpheart.00553.2013).

[9] Biere, L., Donal, E., Terrien, G., Kervio, G., Willoteaux, S., Furber, A. & Prunier, F. 2014 Longitudinal strain is a marker of microvascular obstruction and infarct size in patients with acute ST-segment elevation myocardial infarction. *PLoS One* **9**, e86959. (doi:10.1371/journal.pone.0086959).

[10] Bauer, M., Cheng, S., Jain, M., Ngoy, S., Theodoropoulos, C., Trujillo, A., Lin, F.C. & Liao, R. 2011 Echocardiographic speckle-tracking based strain imaging for rapid cardiovascular phenotyping in mice. *Circ Res* **108**, 908-916. (doi:10.1161/CIRCRESAHA.110.239574).

[11] Wu, V.C., Takeuchi, M., Otani, K., Haruki, N., Yoshitani, H., Tamura, M., Abe, H., Lin, F.C. & Otsuji, Y. 2013 Effect of through-plane and twisting motion on left ventricular strain calculation: direct comparison between two-dimensional and three-dimensional speckle-tracking

echocardiography. *J Am Soc Echocardiogr* **26**, 1274-1281 e1274. (doi:10.1016/j.echo.2013.07.006).

[12] Li, Y., Garson, C.D., Xu, Y., Helm, P.A., Hossack, J.A. & French, B.A. 2011 Serial ultrasound evaluation of intramyocardial strain after reperfused myocardial infarction reveals that remote zone dyssynchrony develops in concert with left ventricular remodeling. *Ultrasound Med Biol* **37**, 1073-1086. (doi:10.1016/j.ultrasmedbio.2011.04.002).

[13] Torres, W.M., Jacobs, J., Doviak, H., Barlow, S.C., Zile, M.R., Shazly, T. & Spinale, F.G. 2018 Regional and temporal changes in left ventricular strain and stiffness in a porcine model of myocardial infarction. *Am J Physiol Heart Circ Physiol* **315**, H958-H967. (doi:10.1152/ajpheart.00279.2018).

[14] Soepriatna, A.H., Damen, F.W., Vlachos, P.P. & Goergen, C.J. 2018 Cardiac and respiratory-gated volumetric murine ultrasound. *Int J Cardiovasc Imaging* **34**, 713-724. (doi:10.1007/s10554-017-1283-z).

[15] Damen, F.W., Berman, A.G., Soepriatna, A.H., Ellis, J.M., Buttars, S.D., Aasa, K.L. & Goergen, C.J. 2017 High-Frequency 4-Dimensional Ultrasound (4DUS): A Reliable Method for Assessing Murine Cardiac Function. *Tomography* **3**, 180-187. (doi:10.18383/j.tom.2017.00016).

[16] Grune, J., Blumrich, A., Brix, S., Jeuthe, S., Drescher, C., Grune, T., Foryst-Ludwig, A., Messroghli, D., Kuebler, W.M., Ott, C., et al. 2018 Evaluation of a commercial multi-dimensional echocardiography technique for ventricular volumetry in small animals. *Cardiovasc Ultrasound* **16**, 10. (doi:10.1186/s12947-018-0128-9).

[17] Ahn, H.S., Kim, Y.K., Song, H.C., Choi, E.J., Kim, G.H., Cho, J.S., Ihm, S.H., Kim, H.Y., Park, C.S. & Youn, H.J. 2017 The impact of preload on 3-dimensional deformation parameters: principal strain, twist and torsion. *Cardiovasc Ultrasound* **15**, 22. (doi:10.1186/s12947-017-0111-x).

[18] Xia, J.Z., Xia, J.Y., Li, G., Ma, W.Y. & Wang, Q.Q. 2014 Left ventricular strain examination of different aged adults with 3D speckle tracking echocardiography. *Echocardiography* **31**, 335-339. (doi:10.1111/echo.12367).

[19] Boyle, J., Soepriatna, A., Damen, F., Rowe, R., Pless, R., Kovacs, A., Goergen, C., Thomopoulos, S. & Genin, G.M. 2018 Accurate and noise insensitive strain mapping enables ultrasound analysis of cardiac function in three dimensions. *J Biomech Eng*. (doi:10.1115/1.4041576).

[20] Satriano, A., Heydari, B., Narous, M., Exner, D.V., Mikami, Y., Attwood, M.M., Tyberg, J.V., Lydell, C.P., Howarth, A.G., Fine, N.M., et al. 2017 Clinical feasibility and validation of 3D principal strain analysis from cine MRI: comparison to 2D strain by MRI and 3D speckle tracking echocardiography. *Int J Cardiovasc Imaging* **33**, 1979-1992. (doi:10.1007/s10554-017-1199-7).

[21] Young, A.A., French, B.A., Yang, Z., Cowan, B.R., Gilson, W.D., Berr, S.S., Kramer, C.M. & Epstein, F.H. 2006 Reperfused myocardial infarction in mice: 3D mapping of late gadolinium

enhancement and strain. *J Cardiovasc Magn Reson* **8**, 685-692. (doi:10.1080/10976640600721767).

[22] Hashmi, S. & Al-Salam, S. 2015 Acute myocardial infarction and myocardial ischemia-reperfusion injury: a comparison. *Int J Clin Exp Pathol* **8**, 8786-8796.

[23] Updegrove, A., Wilson, N.M., Merkow, J., Lan, H., Marsden, A.L. & Shadden, S.C. 2017 SimVascular: An Open Source Pipeline for Cardiovascular Simulation. *Ann Biomed Eng* **45**, 525-541. (doi:10.1007/s10439-016-1762-8).

[24] Chernak Slane, L. & Thelen, D.G. 2014 The use of 2D ultrasound elastography for measuring tendon motion and strain. *J Biomech* **47**, 750-754. (doi:10.1016/j.jbiomech.2013.11.023).

[25] O'Connell, G.D., Johannessen, W., Vresilovic, E.J. & Elliott, D.M. 2007 Human internal disc strains in axial compression measured noninvasively using magnetic resonance imaging. *Spine (Phila Pa 1976)* **32**, 2860-2868. (doi:10.1097/BRS.0b013e31815b75fb).

[26] Cerqueira, M.D., Weissman, N.J., Dilsizian, V., Jacobs, A.K., Kaul, S., Laskey, W.K., Pennell, D.J., Rumberger, J.A., Ryan, T., Verani, M.S., et al. 2002 Standardized myocardial segmentation and nomenclature for tomographic imaging of the heart. A statement for healthcare professionals from the Cardiac Imaging Committee of the Council on Clinical Cardiology of the American Heart Association. *Circulation* **105**, 539-542. (doi:10.1161/hc0402.102975).

[27] Diwan, A., Krenz, M., Syed, F.M., Wansapura, J., Ren, X., Koesters, A.G., Li, H., Kirshenbaum, L.A., Hahn, H.S., Robbins, J., et al. 2007 Inhibition of ischemic cardiomyocyte apoptosis through targeted ablation of Bnip3 restrains postinfarction remodeling in mice. *J Clin Invest* **117**, 2825-2833. (doi:10.1172/JCI32490).

[28] Schneider, C.A., Rasband, W.S. & Eliceiri, K.W. 2012 NIH Image to ImageJ: 25 years of image analysis. *Nat Methods* **9**, 671-675. (doi:10.1038/nmeth.2089).

[29] Thevenaz, P. & Unser, M. 2007 User-friendly semiautomated assembly of accurate image mosaics in microscopy. *Microsc Res Tech* **70**, 135-146. (doi:10.1002/jemt.20393).

[30] Nascimento, D.S., Valente, M., Esteves, T., de Pina Mde, F., Guedes, J.G., Freire, A., Quelhas, P. & Pinto-do, O.P. 2011 MIQuant--semi-automation of infarct size assessment in models of cardiac ischemic injury. *PLoS One* **6**, e25045. (doi:10.1371/journal.pone.0025045).

[31] Humphrey, J.D. 2002 Cardiac Mechanics. *Cardiovascular Solid Mechanics: Cells, Tissues, and Organs* 599-729. New York, Springer-Verlag. (doi:10.1007/978-0-387-21576-1).

[32] Geyer, H., Caracciolo, G., Abe, H., Wilansky, S., Carerj, S., Gentile, F., Nesser, H.J., Khandheria, B., Narula, J. & Sengupta, P.P. 2010 Assessment of myocardial mechanics using speckle tracking echocardiography: fundamentals and clinical applications. *J Am Soc Echocardiogr* **23**, 351-369; quiz 453-355. (doi:10.1016/j.echo.2010.02.015).

[33] Richardson, W.J. & Holmes, J.W. 2016 Emergence of Collagen Orientation Heterogeneity in Healing Infarcts and an Agent-Based Model. *Biophys J* **110**, 2266-2277. (doi:10.1016/j.bpj.2016.04.014).

[34] Fomovsky, G.M., Rouillard, A.D. & Holmes, J.W. 2012 Regional mechanics determine collagen fiber structure in healing myocardial infarcts. *J Mol Cell Cardiol* **52**, 1083-1090. (doi:10.1016/j.yjmcc.2012.02.012).

[35] Van De Water, L., Varney, S. & Tomasek, J.J. 2013 Mechanoregulation of the Myofibroblast in Wound Contraction, Scarring, and Fibrosis: Opportunities for New Therapeutic Intervention. *Adv Wound Care (New Rochelle)* **2**, 122-141. (doi:10.1089/wound.2012.0393).

[36] Preda, M.B. & Burlacu, A. 2010 Electrocardiography as a tool for validating myocardial ischemia-reperfusion procedures in mice. *Comp Med* **60**, 443-447.

[37] Thibault, H., Gomez, L., Donal, E., Pontier, G., Scherrer-Crosbie, M., Ovize, M. & Derumeaux, G. 2007 Acute myocardial infarction in mice: assessment of transmurality by strain rate imaging. *Am J Physiol Heart Circ Physiol* **293**, H496-502. (doi:10.1152/ajpheart.00087.2007).

[38] Gao, X.M., White, D.A., Dart, A.M. & Du, X.J. 2012 Post-infarct cardiac rupture: recent insights on pathogenesis and therapeutic interventions. *Pharmacol Ther* **134**, 156-179. (doi:10.1016/j.pharmthera.2011.12.010).

[39] Hankiewicz, J.H., Goldspink, P.H., Buttrick, P.M. & Lewandowski, E.D. 2008 Principal strain changes precede ventricular wall thinning during transition to heart failure in a mouse model of dilated cardiomyopathy. *Am J Physiol Heart Circ Physiol* **294**, H330-336. (doi:10.1152/ajpheart.01109.2007).

[40] Wells, R.G. 2013 Tissue mechanics and fibrosis. *Biochim Biophys Acta* **1832**, 884-890. (doi:10.1016/j.bbadis.2013.02.007).

[41] Pilla, J.J., Koomalsingh, K.J., McGarvey, J.R., Witschey, W.R., Dougherty, L., Gorman, J.H., 3rd & Gorman, R.C. 2015 Regional myocardial three-dimensional principal strains during postinfarction remodeling. *Ann Thorac Surg* **99**, 770-778. (doi:10.1016/j.athoracsur.2014.10.067).

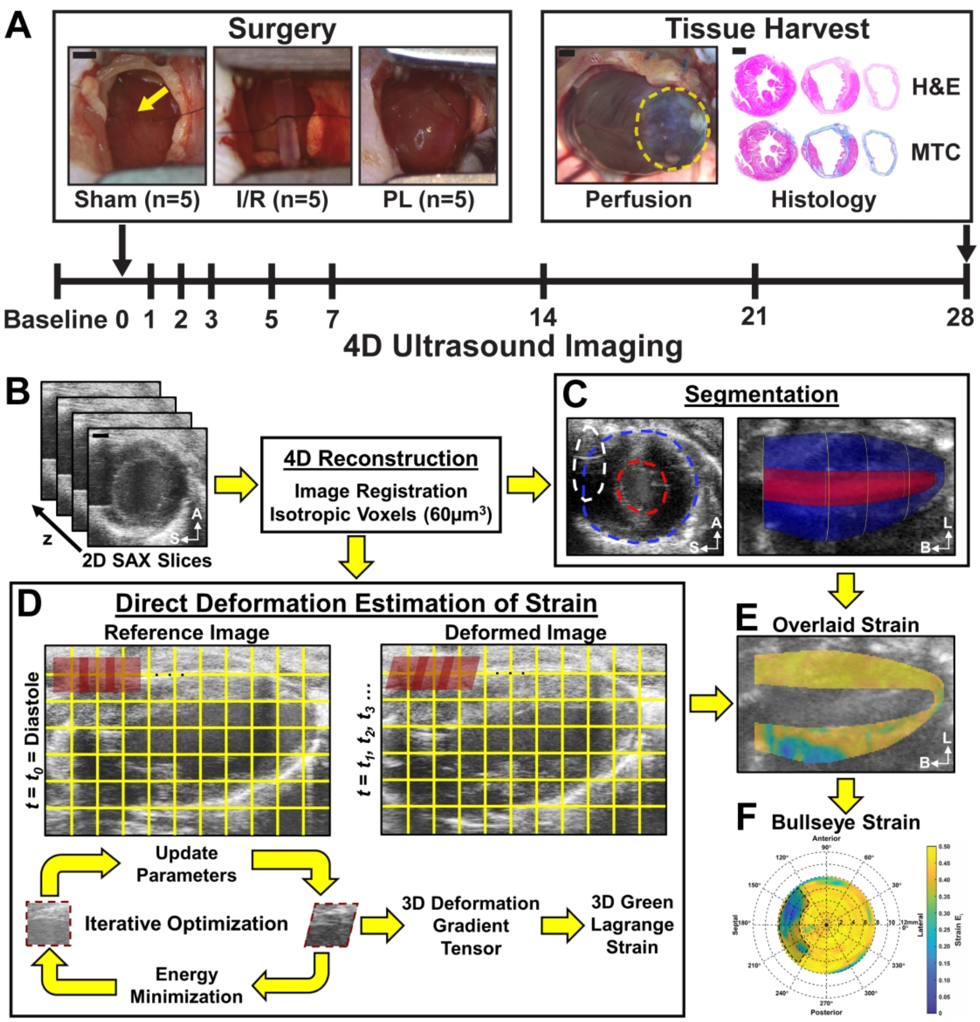

Fig. 1: Study design. **(A)** Fifteen adult, male mice were randomly assigned into 3 surgical groups: 1) sham-operated controls, 2) 30-min ischemia-reperfusion (I/R), and 3) permanent ligation (PL) of the left coronary artery (yellow arrow). A Vevo2100 ultrasound system was used to acquire 4D ultrasound data and flow information of the LV at baseline and on days 1, 2, 3, 5, 7, 14, 21, and 28 post-surgery. At the end of the study, the heart was stained with hematoxylin-eosin (H&E) and Masson's trichrome (MTC). Yellow dashed outlines highlight the infarcted myocardium. **(B)** We reconstructed 4D ultrasound data from ECG and respiratory-gated 2D short-axis ultrasound images of the LV. **(C)** 3D endocardial (red), epicardial (blue), and sternal artifact (white) boundaries were segmented at end-diastole and peak-systole. **(D)** Maximum principal 3D Green-Lagrange strain (E_I) was calculated using a direct deformation estimation technique. **(E)** Strain was then localized within the myocardium using segmented boundaries and presented as bullseye maps **(F)**. A: anterior, S: septal, L: lateral; B: base. Scalebar: 1mm.

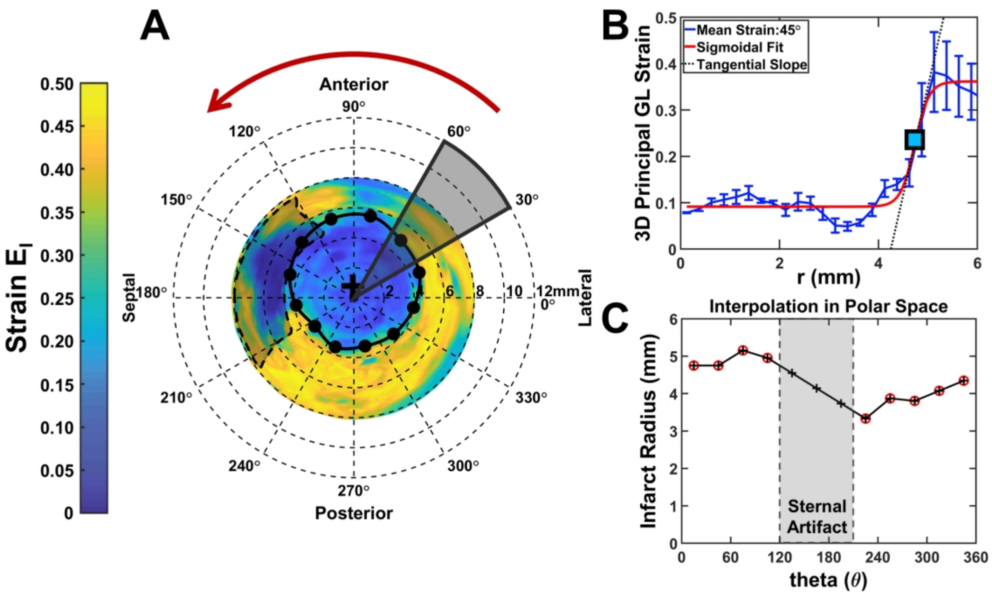

Fig. 2: Strain estimation of infarct size. **(A)** We extracted myocardial strain profiles radially from the infarct center (black crosshair) and performed sigmoidal fitting on strain profiles averaged across every 30° region. **(B)** The spatial positions of the inflection points (square box and black dots) are defined as the infarct border and unwrapped from the infarct center to estimate infarct boundaries in regions with sternal artifacts **(C)**. Infarct size is defined as the percentage of the myocardium that lies within the strain-estimated infarct boundary.

203x120mm (300 x 300 DPI)

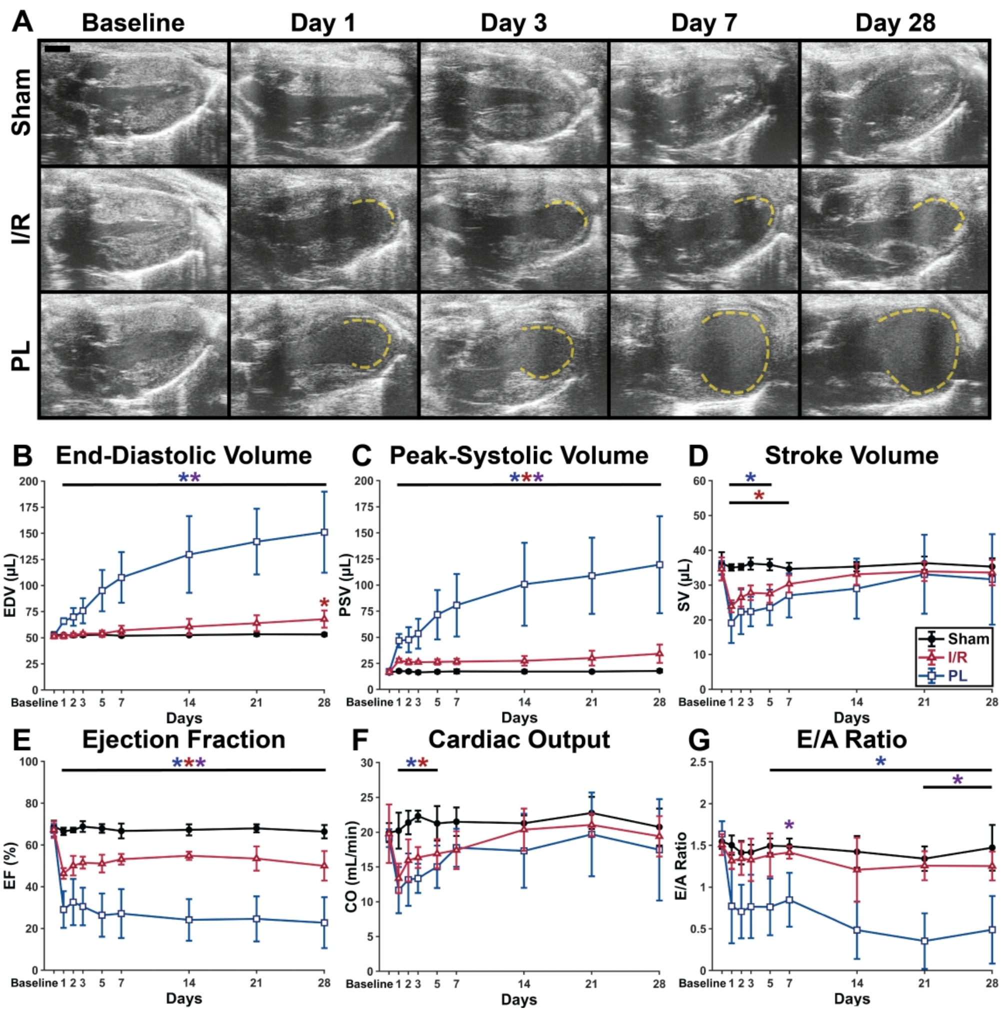

Fig. 3: LV remodeling post-infarction. **(A)** Representative long-axis ultrasound images of mouse LVs taken at peak-systole. Akinetic myocardial walls, indicative of ischemic damage, are outlined in dashed yellow lines. Global metrics of LV function **(B-G)** showed that mice in both I/R and PL groups exhibited significant reductions in LV contractile function post-surgery, but significant dilation and diastolic dysfunction were only consistently measured in the PL group. Taken together, mice in the PL group experienced greater degrees of cardiac remodeling when compared to those in the I/R group. Data are shown as mean ± standard deviations (**p*<0.05). I/R: ischemia-reperfusion, PL: permanent ligation. Blue asterisks: PL vs. Sham; Red asterisks: I/R vs. Sham; Purple asterisks: PL vs. I/R. Scalebar: 1mm.

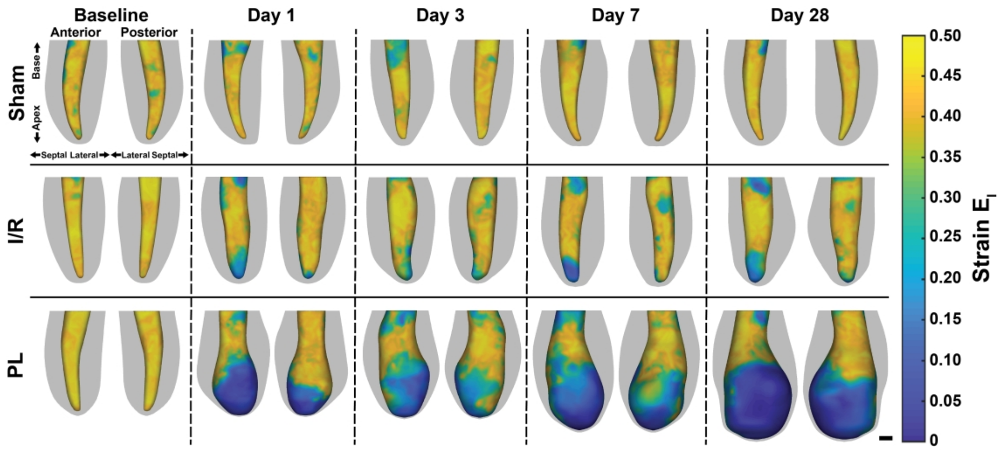

Fig. 4: Longitudinal 3D representations of peak-systolic LV boundaries with maximum principal 3D Green-Lagrange myocardial strains (E_I) overlaid onto the endocardial wall. Epicardial boundaries are shown in gray. Dark blue areas highlight akinetic regions of the myocardium. Scalebar: 1mm.

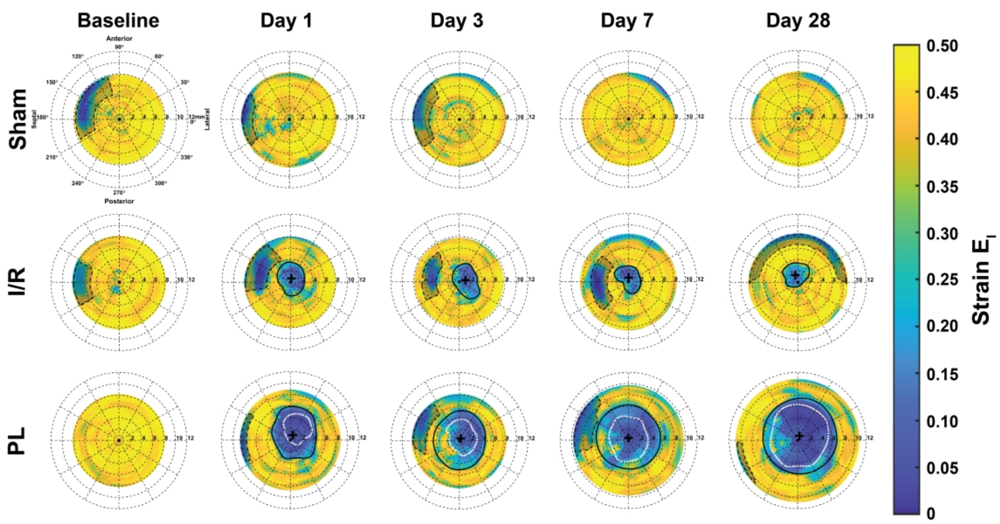

Fig. 5: Longitudinal bullseye maps of the maximum principal 3D Green-Lagrange strain (E_I) within the myocardium. Strain-estimated infarct boundaries are outlined in solid black lines with infarct centers marked as black crosshairs. Wall-thinned infarct boundaries measured from segmentation are outlined as white dotted lines, while sternal artifacts are outlined as black dashed lines.

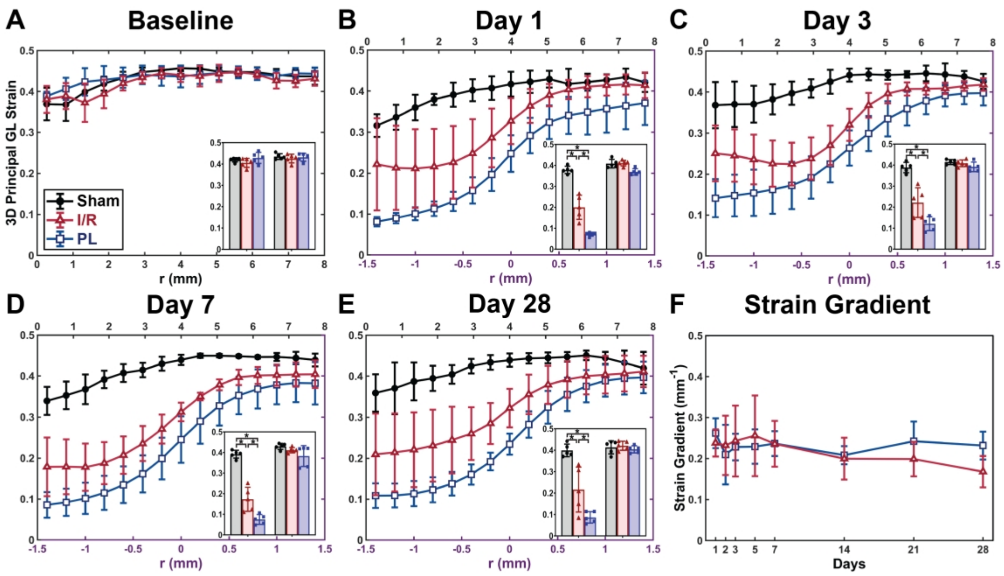

Fig. 6: Myocardial strain profiles of the remodeling LVs averaged across mice in each group and plotted at **(A)** baseline and **(B-E)** on days 1, 3, 7, and 28 post-surgery. Strain profiles in nonischemic mice (baseline and sham) are plotted radially away from the LV apex (black x-axis). In ischemic mice, strain profiles are plotted only in regions near infarct boundaries (r = 0; purple x-axis). Strain values averaged within the infarcted and remote myocardium are shown as the left and right inset bar graphs respectively. **(F)** Strain gradients, calculated within the linear component of the sigmoidal fit from the strain profiles, did not show significant changes between surgical groups over the 28-day period. Data are shown as mean ± standard deviations (*$p<0.05$).

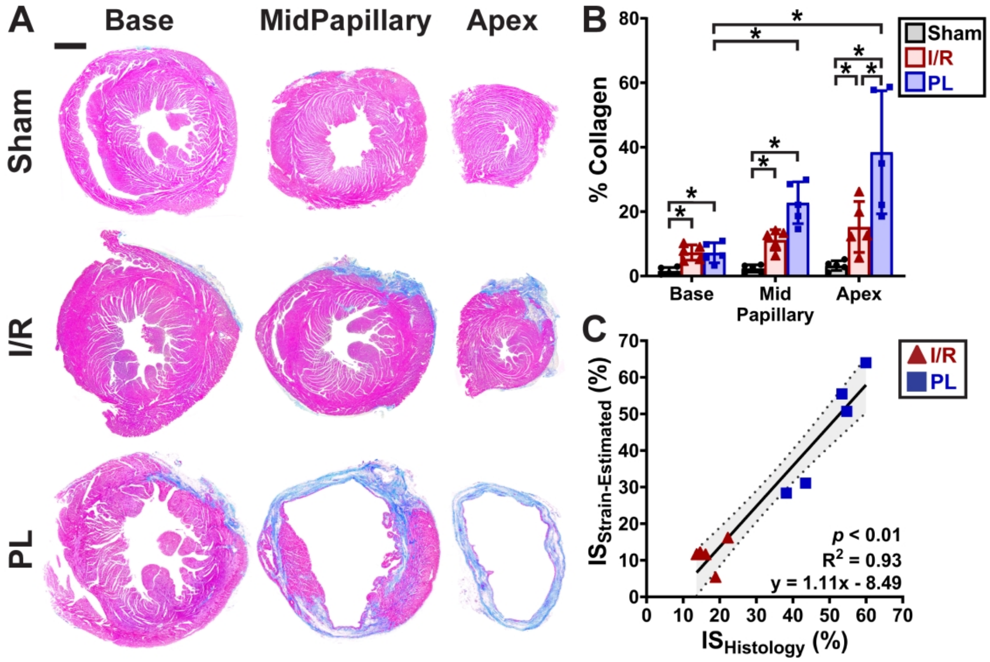

Fig. 7: Histological analysis of collagen content and infarct size. **(A)** Histology images of mouse LVs, obtained 28 days post-surgery and stained with Masson's Trichrome, revealed subepicardial scarring in the I/R group and transmural infarcts in the PL group. Muscle fibers are stained red while collagen-rich scars are stained blue. **(B)** Bar graphs showing percent collagen highlighted spatial variations in collagen content relative to infarct location. **(C)** Strain-estimated infarct size strongly correlated to infarct size measured from the histological midline length approach. Data are shown as mean ± standard deviations (*$p<0.05$). Scalebar: 1mm.

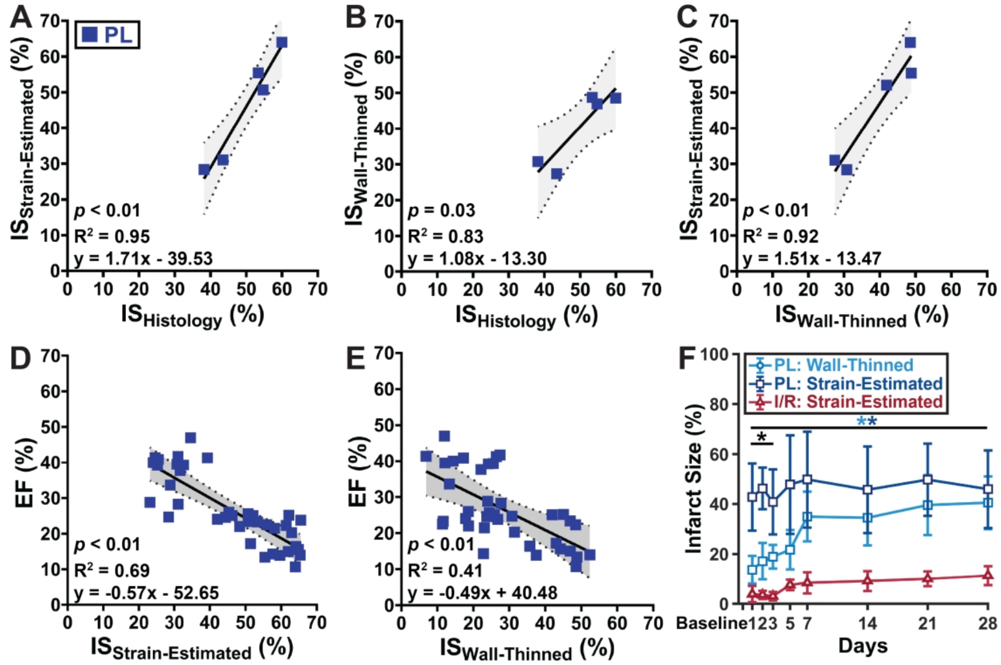

Fig. 8: Correlation of varying infarct sizing techniques with cardiac function. **(A-C)** Correlation plots comparing three different infarct sizing methodologies showed that the proposed strain-estimation technique best correlated with gold-standard histological estimation of infarct size. Correlation of **(D)** strain-estimated and **(E)** wall-thinned infarct size with ejection fraction. Linear regression lines are shown as solid black lines with 95% confidence intervals shaded in gray. **(F)** Line graphs summarizing infarct size growth throughout cardiac remodeling. Data are shown as mean ± standard deviations (*$p<0.05$). Light blue asterisks: wall-thinned PL vs. strain-estimated I/R; Dark blue asterisks: strain-estimated PL vs. strain-estimated I/R; Black asterisks: wall-thinned PL vs. strain-estimated PL.